

Magic wavelengths of the Sr ($5s^2\ ^1S_0$ – $5s5p\ ^3P_1$) intercombination transition near the $5s5p\ ^3P_1$ – $5p^2\ ^3P_2$ transition

Grady Kestler¹,[✉] Khang Ton,¹ Dmytro Filin,² Marianna S. Safronova,² and Julio T. Barreiro¹

¹*Department of Physics and Astronomy, University of California, San Diego, California 92093, USA*

²*Department of Physics and Astronomy, University of Delaware, Newark, Delaware 19716, USA*



(Received 18 November 2021; accepted 18 January 2022; published 31 January 2022)

Predicting magic wavelengths accurately requires precise knowledge of electric dipole matrix elements of nearby atomic transitions. As a result, measurements of magic wavelengths allow us to test theoretical predictions for the matrix elements that frequently cannot be probed by any other methods. Here, we calculate and measure a magic wavelength near 473 nm of the $5s^2\ ^1S_0$ – $5s5p\ ^3P_1$ intercombination transition of ^{88}Sr . Experimentally, we find 473.371(6) nm for $\Delta m = 0$ (π transition) and 473.117(15) nm for $\Delta m = -1$ (σ^- transition). Theoretical calculations yield 473.375(22) and 473.145(20) nm, respectively. Determining magic wavelengths nearby the dominant 461-nm probe transition of ^{88}Sr holds promise for state insensitive interfacing of strontium atoms and nanophotonic devices with a narrow band of operating wavelengths. Furthermore, the 3P_1 polarizability is dominated by the contributions to the $5p^2\ ^3P$ levels, and excellent agreement of theory and experiment validates both theoretical values of these matrix elements and estimates of their uncertainties.

DOI: [10.1103/PhysRevA.105.012821](https://doi.org/10.1103/PhysRevA.105.012821)

I. INTRODUCTION

Laser cooling and probing of atoms trapped in optical potentials, such as in optical dipole traps (ODTs), have been powerful tools for quantum science and technology, e.g., for optical atomic clocks [1,2]. These tools rely on lasers driving an atomic optical transition between two electronic energy levels. In a dipole trap, these two levels have different atomic polarizabilities, resulting in different AC Stark energy-level shifts as well as level-dependent optical forces. Consequently, the effectiveness of laser cooling and probing depends on the location of the atoms in the heterogeneous intensity of the optical fields.

Depending on the atomic electronic structure, it is possible to overcome such challenges by tuning the ODT beam to so-called *magic* wavelengths, inducing the same atomic polarizability in each of the two levels [3–5]. In the context of probing optical transitions of trapped atoms, magic-wavelength traps have enabled many improvements, such as precision spectroscopy [6,7], the most accurate and stable optical atomic clocks to date [2,8,9], and the reduction of decoherence effects in the quantum gates of a quantum computer based on neutral atoms [10–13].

In the context of laser cooling, using magic-wavelength traps enables a more efficient transfer of atoms from a magneto-optical trap (MOT) into optical “tweezers” [14,15], ODTs in which the trap diameter is of the same order as the trapping wavelength [5,16,17]. These traps operate in a regime of large intensities and, thus, large differential AC Stark shifts, which are eliminated by using magic wavelengths.

The same principles and improvements for optical tweezers can be applied to interfacing cold atoms with nanoscale waveguides for enhanced atom-photon interactions [14,18].

Prominent applications of such systems include cavity quantum electrodynamics [6,19] and quantum many-body emulations with tunable interaction strengths [20,21]. In these platforms, the fields inside the nanophotonic waveguides can give rise to high intensity evanescent trapping fields near the free-space surface of the device. Hybrid systems, such as nanotapered optical fiber traps have already benefited from magic wavelengths by increasing their coherence times through the elimination of spatially dependent energy shifts near the fiber surface [22,23]. Furthermore, unlike free-space trapping methods, a repulsive evanescent field is also necessary to counteract the Casimir Polder potential near nanophotonic surfaces. The attractive light field then requires intensities typically more than twice larger than trapping in free space, thus, giving rise to larger AC Stark shifts for off-magic trapping wavelengths.

Most of the current experiments have successfully interfaced cesium [18,22,24] or rubidium atoms [25–27] with photonic waveguides. However, the bosonic isotope of strontium ^{88}Sr has several advantages [7]. It is less susceptible to magnetic fields due to a spherically symmetric ground state and no electronic or nuclear spin. Compared to other atomic species or strontium isotopes, this isotope also has a smaller collisional scattering length, thus, minimizing any dephasing effects in matter-wave interferometry. Furthermore, with strontium, the easily achievable single-digit micro-Kelvin temperatures allow us to trap and perform spectroscopy with milliwatts of optical power instead of watts [28], even after accounting for differing contributions to trapping strengths.

An initial step towards efficiently loading ^{88}Sr into nanophotonic evanescent fields is to identify magic wavelengths of the narrow-line intercombination cooling transition that leads to micro-Kelvin temperatures. However, there is an

added complication with photonic devices, e.g., optical ring resonators whereby they are difficult to design for strongly guided modes across a wide range of wavelengths. Probing trapped ^{88}Sr atoms from the nanowaveguide with the dominant $5s^2\ ^1S_0 - 5s5p\ ^1P_1$ (henceforth, $^1S_0 - ^1P_1$) transition at ≈ 461 nm, drives the material choices of the photonic devices for operation in the blue spectrum, and this, in turn, the choice of trapping magic wavelengths. Current state insensitive trapping of ^{88}Sr makes use of magic wavelengths at ≈ 515 [5] and ≈ 813 nm [7] both of which are difficult to accommodate in a device tuned for the blue spectrum.

Here we calculate and experimentally verify magic wavelengths of the $5s^2\ ^1S_0 - 5s5p\ ^3P_1$ (henceforth, $^1S_0 - ^3P_1$) intercombination transition of ^{88}Sr .

II. THEORY

For a linearly polarized laser field, the differential AC Stark shift between a ground and an excited state is proportional to the differential atomic polarizability $\Delta\alpha = (\alpha_e - \alpha_g)$ and the intensity I of the light field $h\Delta f \propto -\Delta\alpha I$, where α_e (α_g) is the atomic polarizability of the ground (excited) state. The polarizability is further separated into its irreducible parts, the scalar, vector, and tensor polarizabilities (α_0 , α_1 , and α_2 , respectively). The scalar component acts as a level-independent shift, and the tensor component has a quadratic dependence on the m_J Zeeman sublevels of the excited state. The vector field is only present with circularly polarized light and behaves in the same capacity as a magnetic Zeeman shift.

The spherically symmetric ground state has zero angular momentum and, thus, only contains the scalar component. The excited state 3P_1 does not have vanishing angular momentum and must include a contribution from the tensor polarizability as well. This contribution depends on the Zeeman substate and a geometric term based on the polarization angle relative to the quantization axis θ_p . We can neglect the vector term completely by considering pure linear polarization. Then the total polarizability becomes [28]

$$\alpha = \alpha_0 + \alpha_2 \left(\frac{3 \cos^2 \theta_p - 1}{2} \right) \frac{3m^2 - J(J+1)}{J(2J-1)}. \quad (1)$$

For $\theta_p = 0$ considered here, $\alpha = \alpha_0 - 2\alpha_2$ for $m = 0$ and $\alpha = \alpha_0 + \alpha_2$ for $|m| = 1$. The magic wavelengths are determined as crossing points of the 1S_0 and 3P_1 polarizability curves for $|m| = 0, 1$.

The frequency-dependent scalar polarizability $\alpha(\omega)$ of an atom in a state v may be separated into a core polarizability and a contribution from the valence electrons. There is no core contribution to the tensor polarizability as angular momentum of the core is zero. The core polarizability is a sum of the polarizability of the ionic Sr^{2+} core and a “vc” term that compensates for a Pauli principle violating core-valence excitation from the core to the valence shells. The core polarizability is small and essentially independent from frequency in the range of interest for this paper, so it is sufficient to use its static value calculated in the random-phase approximation (RPA) [29].

We calculate the valence polarizabilities using a hybrid approach that combines configuration iteration and a linearized coupled-cluster method (CI + all order) [29,32,33]. The valence part of the polarizability for state v with the total angular

momentum J and projection m is determined by solving the inhomogeneous equation of perturbation theory in the valence space, which is approximated as [34]

$$(E_v - H_{\text{eff}})|\Psi(v, m')\rangle = D_{\text{eff},g}|\Psi_0(v, J, m)\rangle. \quad (2)$$

The parts of the wave-function $\Psi(v, m')$ with angular momenta of $J' = J, J \pm 1$ are then used to determine the scalar and tensor polarizabilities. The effective Hamiltonian H_{eff} used in the configuration interaction (CI) calculations includes the all-order corrections calculated using the linearized coupled-cluster method with single and double excitations. The effective dipole operator D_{eff} includes RPA corrections. This approach automatically includes contributions from all possible states.

The magic wavelengths of interest are very close to the resonances, the wavelength of the $5s5p\ ^3P_1 - 5p^2\ ^3P_2$ transition is 472.4 nm, and it is essential that such relevant transition energies are accurate in a polarizability computation. Therefore, we extract several contributions to the valence polarizabilities using the sum-over-states formulas [35],

$$\begin{aligned} \alpha_0^v(\omega) &= \frac{2}{3(2J+1)} \sum_k \frac{\langle k|D|v\rangle^2 (E_k - E_v)}{(E_k - E_v)^2 - \omega^2}, \\ \alpha_2^v(\omega) &= -4C \sum_k (-1)^{J+j_k+1} \begin{Bmatrix} J & 1 & j_k \\ 1 & J & 2 \end{Bmatrix} \\ &\quad \times \frac{\langle k|D|v\rangle^2 (E_k - E_v)}{(E_k - E_v)^2 - \omega^2}, \end{aligned} \quad (3)$$

where a quantity in $\{ \}$ brackets is a Wigner 6- j symbol and j_k as the total angular momentum of the state k . The value of C is given by

$$C = \left(\frac{5J(2J-1)}{6(J+1)(2J+1)(2J+3)} \right)^{1/2}.$$

We replace such contributions with values obtained using the experimental energies [30] and recommended values of the matrix elements from Refs. [29,31,32,36]. In more detail, we first calculate four such contributions for the 1S_0 polarizability and 15 contributions for the 3P_1 polarizability using *ab initio* energies and matrix elements that exactly correspond to our calculations using the inhomogeneous equation (2) and determine the remainder contribution of all other states. Then, we compute the same terms using the experimental energies [30] and recommended values of matrix elements from Refs. [29,31,32,36]. Theoretical values of the matrix elements are retained where recommended values are not available. The recommended value for the $^1S_0 - ^1P_1$ matrix element is from the 1P_1 lifetime measurement [31] but with increased uncertainty based on the discussion in Ref. [32]. After this procedure, we add the core and the remainder contribution from the other states to these values to obtain the final results. This calculation is illustrated by Tables I and II where we list contributions to the 1S_0 and 3P_1 polarizabilities in atomic units at the 473.1445- and 473.375-nm $^1S_0 - ^3P_1$ magic wavelengths. Transition energies ΔE [30] in cm^{-1} and the recommended value of the electric dipole matrix elements D [29,31,32,36] (in atomic units) are also listed. The breakdown of the

TABLE I. Contributions to the $5s^2\ ^1S_0$ polarizability in atomic units at the 473.1445- and 473.375-nm $^1S_0 - ^3P_1$ magic wavelengths. Transition energies ΔE [30] in cm^{-1} and the value of the electric dipole matrix element D [31,32] (in atomic units) are also listed.

Contributions	ΔE	D	α_0	α_0
			473.1445 nm	473.375 nm
$5s5p\ ^1P_1$	21698	5.248(12)	3624(17)	3560(16)
Other			8	8
Core + vc			5	5
Total			3637(17)	3573(16)

contributions shows that the 3P_1 polarizability is strongly dominated by the contributions from the $5s5p\ ^3P_1 - 5p^2\ ^3P_1$ transitions.

The determination of the magic wavelengths and their uncertainties is illustrated in Fig. 1, where we plot the calculated polarizabilities for $5s^2\ ^1S_0$ and $5s5p\ ^3P_1$, $|m| = 0, 1$ states. The magic wavelengths are obtained as the crossing points. We determine the uncertainty of all polarizability contributions from the estimated uncertainties in the values of the matrix elements, adding all uncertainties in quadrature. We plot $\alpha + \delta\alpha$ and $\alpha - \delta\alpha$ for all levels and determine the uncertainty in the values of the magic wavelength from crossings of these additional curves. The final values are in excellent agreement with the experiment, confirming the central values and the 1% estimated uncertainties of the $5s5p\ ^3P_1 - 5p^2\ ^3P_1$ matrix elements.

III. EXPERIMENTAL METHODS

Cold atoms are prepared in our experiment [37] using established laser cooling techniques for strontium [38,39] (see the Appendix). At the end of the narrow-line “red” MOT cooling stage, see Fig. 2(a), we capture around 5×10^5 atoms at $\approx 1\ \mu\text{K}$. The ODT beam is then overlapped with the cold

TABLE II. Contributions to the $5s5p\ ^3P_1$ polarizability in atomic units at the 473.1445- and 473.375-nm $^1S_0 - ^3P_1$ magic wavelengths. Transition energies ΔE in cm^{-1} [30] and the recommended values of the electric dipole matrix elements D (see the text) in atomic units, are also listed. $5s5p\ ^3P_1\ |m| = 1$ polarizabilities are obtained as $\alpha(|m| = 1) = \alpha_0 + \alpha_2$; $m = 0$ polarizabilities are obtained as $\alpha(m = 0) = \alpha_0 - 2\alpha_2$.

Contributions	ΔE	D	α_0	α_2	$\alpha(m = 1)$	α_0	α_2	$\alpha(m = 0)$
			$\lambda = 473.1445\ \text{nm}$			$\lambda = 473.375\ \text{nm}$		
$5s4d\ ^3D_1$	3655	2.318(5)	-2	-1	-3	-2	-1	0
$5s4d\ ^3D_2$	3714	4.013(9)	-7	1	-6	-7	1	-8
$5s6s\ ^3S_1$	14534	3.435(14)	-36	-18	-53	-36	-18	0
$5s5d\ ^3D_1$	20503	2.005(20)	-153(3)	-76(2)	-229	-155(3)	-78(2)	0
$5s5d\ ^3D_2$	20518	3.671(36)	-524(10)	52(1)	-472	-533(10)	53(1)	-640
$5p^2\ ^3P_0$	20689	2.658(27)	-382(8)	382(8)	0	-391(8)	391(8)	-1174
$5p^2\ ^3P_1$	20896	2.363(24)	-565(11)	-283(6)	-848	-591(12)	-296(6)	0
$5p^2\ ^3P_2$	21170	2.867(29)	5714(116)	-571(12)	5142	4420(89)	-442(9)	5304
$5p^2\ ^1D_2$	22457	0.228(11)	1	0	1	1	0	1
$5p^2\ ^1S_0$	22656	0.291(15)	1	-1	0	1	-1	4
$5s7s\ ^3S_1$	22920	0.921(28)	12(1)	6	18	12(1)	6	0
Other			81(2)	1	82	81(2)	1	80
Core + vc			6		6	6		6
Total			4146(117)	-509(15)	3637(118)	2805(91)	-384(14)	3573(92)

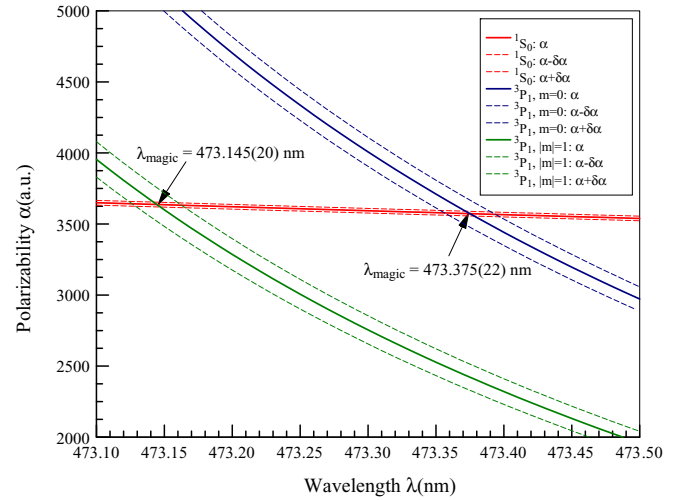
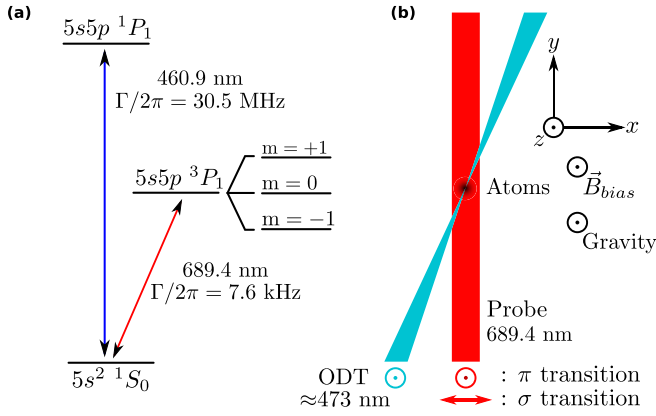


FIG. 1. Calculated polarizabilities for $5s^2\ ^1S_0$ and $5s5p\ ^3P_1$, $m = 0$, and $|m| = 1$ levels and corresponding magic wavelengths.

atomic cloud as shown in Fig. 2(b). For detection, a 689-nm laser beam is scanned in frequency to probe the $^1S_0 - ^3P_1$ narrow-line transition for spin-resolved atomic absorption imaging.

The magic wavelength is determined by measuring the differential AC Stark shift at wavelengths both above and below the predicted magic value. First, a reference spectroscopic scan without the ODT is performed at 1 ms after the atoms are released from the ODT. Then, at ODT powers between 20 and 70 mW, corresponding to trap depths between 2 and 10 μK , we measure the shift in the resonance due to the presence of the ODT beam [Fig. 3(a)]. The slope which characterizes the linear relationship of the detuning and trapping powers is defined as the differential Stark shift coefficient (DSSC) and given by $\Delta f/P$, where Δf is the differential AC Stark shift and P is the ODT power [Fig. 3(b)]. For positive (negative) DSSC, the differential AC Stark shift will increase (decrease) with increasing powers and is zero at the magic wavelength.



Spin-resolved spectroscopy is achieved by applying a large bias magnetic-field $B_{\text{bias}} = 200(11)$ mG in the $+z$ direction. This separates the excited state Zeeman levels by 420 kHz

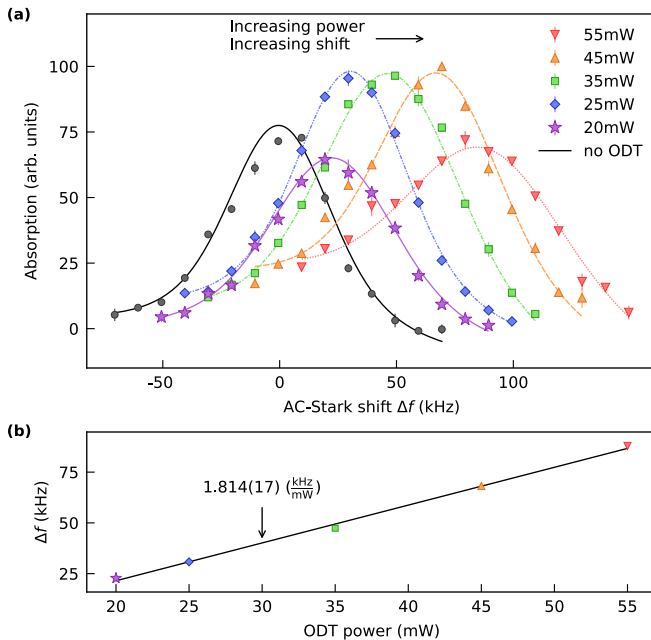
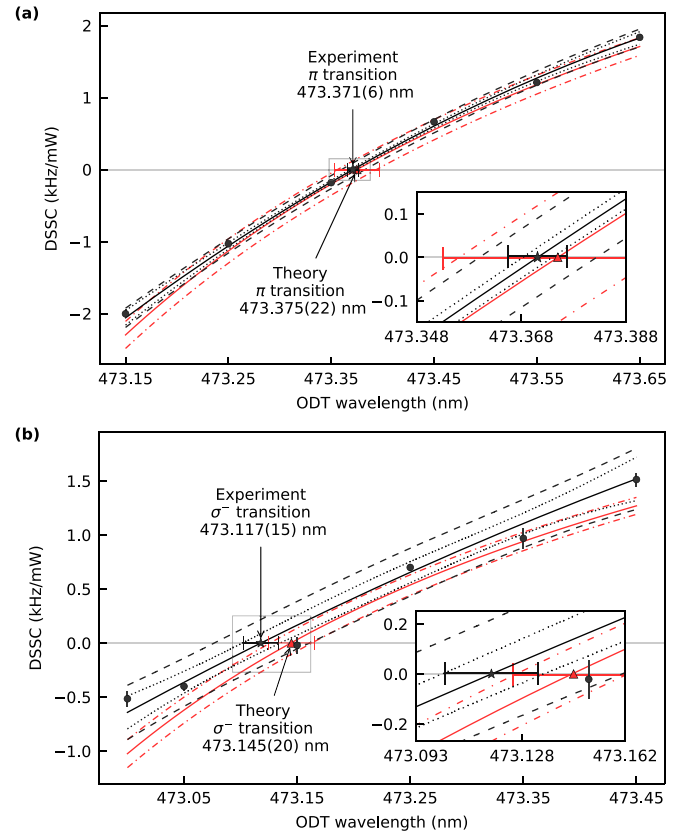


FIG. 3. (a) Sample absorption spectroscopy scans for varying powers of an ODT at a wavelength of 473.65 nm for the π transition. The AC Stark shift axis is centered with respect to a reference scan without ODT (black solid line). Each scan is fitted to a Voigt plus linear model (see the Appendix). (b) AC Stark shift vs ODT power. At this wavelength, the Voigt centers increase in frequency with the ODT beam power and result in a positive differential Stark shift coefficient (DSSC).



providing sufficient splitting of the $m = 0$ and $m = -1$ resonances, whose widths are primarily limited by Doppler broadening on the order of 30 kHz. Additionally, the probe beam polarization is set to vertical (π) or horizontal (σ) depending on the measurement [Fig. 2(b)]. Since $m = -1$ measurements are sensitive to magnetic fields (2.1 kHz/mG), we perform an additional second resonance scan after two of the five ODT powers to ensure the bias field is stable.

The ODT polarization is chosen to be vertical and parallel ($\theta_p = 0$) to the quantization axis defined by the \vec{B}_{bias} consistent with the theoretical predictions. This guarantees the excited-state polarizabilities for the Zeeman sublevels are given by $\alpha = \alpha_0 - 2\alpha_2$ for $m = 0$ and $\alpha = \alpha_0 + \alpha_2$ for $|m| = 1$. Measuring both differential polarizabilities allows us to separate and recombine the scalar and tensor polarizabilities for any θ_p [28].

TABLE III. Various contributions to the magic wavelength measurement error in picometers. Statistical errors, ODT power fluctuations, and atom count fluctuations are propagated through the fitting procedure and included in the measurement error row. All contributions and corrections are accounted for in Fig. 4.

Contribution	Offset		Uncertainty	
	π	σ^-	π	σ^-
Measurement	0	0	4	14
θ_p	+10	-15	4	6
Wavemeter	+0.4	+0.4	0.1	0.1
Total	+10.4	-14.6	6	15

IV. RESULTS AND DISCUSSION

With the DSSC measurements at each wavelength of Fig. 4, the data (black) exhibits a quadratic behavior due to the proximity of the nearby excited-state resonance at 472.4 nm. Thus, we fit the experimental data to a quadratic model (Fig. 4). We calculate the magic wavelength at the zero crossing by employing a root finding Monte Carlo approach, which gives 473.371(6) nm for $m = 0$ and 473.117(15) nm for $m = -1$.

The theoretical calculation of the differential polarizability $\Delta\alpha$ relates to the DSSC by $\Delta f = 1/(2h\epsilon_0 c)I\Delta\alpha$ where the beam intensity for a Gaussian beam $I = 2P/(\pi w^2)$ depends on the beam waist at the atoms w . In Fig. 4 (red) we fit the theoretical differential polarizability to our data leaving the beam waist as a free parameter. At the magic wavelength, the differential polarizability is zero and independent of beam waist. The fit is consistent with the theoretical prediction, providing a beam waist of $w = 44(2)\ \mu\text{m}$ for π polarization and $w = 58(1)\ \mu\text{m}$ for σ^- polarization, similar to out-of-vacuum measurements for each independent experiment. The red dashed-dot lines are theoretical $\delta\alpha$ uncertainties from Fig. 1.

There is a systematic error produced by an offset of θ_p from 0 and is already accounted for in Fig. 4. We measure θ_p using an indirect method by comparing the excited-state populations of the π and σ^- transitions [28] (see the Appendix). We find the angle to be $15 \pm 6^\circ$ from 0 corresponding to a shift in the magic wavelengths of +10 pm for the π transition and -15 pm for the σ^- transition. A summary of systematic errors and uncertainties are compiled in Table III.

V. CONCLUSION

In this paper, we report on our investigation of magic wavelengths of the $5s^2\ ^1S_0-5s5p\ ^3P_1$ intercombination transition of ^{88}Sr . By inducing a Zeeman splitting of the excited state, we measure one magic wavelength for the $\Delta m = 0$ (π transition) and another for the $\Delta m = -1$ (σ^- transition). Precision atomic calculations predicts values of 473.375(22) nm (π) and 473.145(20) nm (σ) that are consistent with our experimental results of 473.371(6) and 473.117(15) nm, respectively. The 3P_1 polarizability is strongly dominated by the contributions from the $5s5p\ ^3P_1-5p^2\ ^3P_J$ transitions for which there are no prior experimental benchmarks. As the 1S_0 polarizability is essentially defined by the experimentally known $^1S_0-^1P_1$ matrix elements, the magic wavelengths

probe $5s5p\ ^3P_1-5p^2\ ^3P_J$ transitions. Excellent agreement of theory and experiment validates both theoretical values of these matrix elements and estimates of their uncertainties.

Employing narrow-line magic wavelengths eliminates position- and level-dependent forces, allowing for more efficient optical trapping. Additionally, the proximity of an attractive ≈ 473 -nm magic trapping wavelength, and a repulsive magic wavelength at ≈ 436 nm, to the $^1S_0-^1P_1$ dominating transition at ≈ 461 nm is key to trapping ^{88}Sr on the evanescent fields of nanoscale waveguides, particularly, with a MOT operating with a narrow-linewidth transition. These evanescent fields often give rise to elliptical polarizations which induce a vector shift of the excited state (3P_1) polarizabilities, something not considered in this paper. However, depending on the geometry of the waveguides in question, compensation schemes [23] can cancel the elliptical components and the results reported here are then applicable.

ACKNOWLEDGMENTS

We would like to thank P. Lauria for helpful insight, discussions, and assistance building the experimental apparatus. We acknowledge the support of the Office of Naval Research under Grants No. N00014-20-1-2513 and No. N00014-20-1-2693 and a UC San Diego Lattimer Faculty Fellowship. This research was supported, in part, through the use of University of Delaware HPC Caviness and DARWIN computing systems: DARWIN: A Resource for Computational and Data-intensive Research at the University of Delaware and in the Delaware Region, R. Eigenmann, B. E. Bagozzi, A. Jayaraman, W. Totten, and C.H. Wu, University of Delaware, 2021 [40].

APPENDIX

1. Experimental setup

In our experiment, strontium atoms are expelled in a collimated atomic beam from an oven heated to 480 °C. The atoms, Doppler shifted due to the high velocity, are slowed by a Zeeman slower composed of a counterpropagating laser beam detuned by $\Delta/2\pi = -540$ MHz from the $^1S_0-^1P_1$ transition and a spatially dependent magnetic field designed to keep atoms on resonance as they are slowed. Two-dimensional MOTs redirect the slowed atomic beam into the main chamber. The strontium oven and optics for the 2D MOT and Zeeman slower are commercial from AOSense Incorporated.

Atoms are then captured in the main chamber with a three-dimensional “blue” MOT, named for the color of the trapping light at ≈ 461 nm. Spatially dependent magnetic-field gradients along each axis impart an energy shift of the excited state Zeeman sublevels dependent on the position of the atoms from the center of the trap. Counterpropagating beams with polarizations set to σ^+ and σ^- are once again detuned at $\Delta/2\pi = -40$ MHz from the $^1S_0-^1P_1$ transition and interact with the off-center atoms further cooling whereas imparting a restoring force for trapping.

During the blue MOT stage, about 1:50 000 atoms in the 1P_1 state decay to the $5s5p\ ^3P_2$ metastable reservoir state. A laser beam tuned to the $5s5p\ ^3P_2-5p^2\ ^3P_2$ transition at 481 nm, repumps the atoms from the metastable state to the

3P_1 where they are further cooled and trapped in the second stage, red MOT, operating on the $^1S_0 - ^3P_1$ transition at ≈ 689 nm using an external cavity diode laser with a linewidth below 1 kHz.

The red MOT stage operates in two phases. The sawtooth wave adiabatic passage technique [41,42] is applied during an initial broadband phase wherein the laser detuning is swept at a rate of 40 kHz in a triangle waveform from $\Delta_-/2\pi = -10$ MHz to $\Delta_+/2\pi = +200$ kHz followed by a lower power single frequency phase with the detuning fixed at $\Delta/2\pi = -290$ kHz. At the end of both phases, we capture 5×10^5 atoms on average.

The temperatures achieved after each MOT stage are limited by the natural linewidth of the relevant transition. The blue MOT ($\Gamma/2\pi = 30.5$ MHz) reaches temperatures on the order of 1 mK and the red MOT ($\Gamma/2\pi = 7.6$ kHz) achieves temperatures of ≈ 1 μ K.

During the red MOT cooling and trapping, the ODT beam is overlapped with the atomic cloud for 100 ms before turning off the MOT beams for 10 ms and taking an absorption image of the atoms. The imaging probe beam operates on the narrow-line 689-nm transition with $I/I_{\text{sat}} = 0.15$ and pulse length of 50 μ s. The absorption imaging light is collected on an Andor 897 EMCCD camera.

The ODT beam is aligned across the center of the red MOT by setting the ODT beam frequency at the resonance frequency of the $5s5p \ ^3P_1 - 5p^2 \ ^3P_2$ transition, determined from the literature to be at 472.36 nm. The ODT beam induces a large AC Stark shift on the atoms rendering them transparent to the MOT cooling beams. As the resonant ODT beam is aligned towards the center of the cold atomic cloud, the number of atoms is minimized. We repeatedly decrease the power and continue alignment until only the atoms in the center of the atomic cloud interact with the ODT beam. When the beam is aligned, a dimple appears in the center of the atomic cloud where no atoms are trapped.

2. Spectroscopy

With the fitted beam waists of 44 and 58 μ m at the atoms for $m = 0$ and $m = -1$ measurements, we calculate the Rayleigh range to be 13 and 22 mm. The atoms are trapped in the ODT in the shape of a narrow cylinder whose length, whereas less than the Rayleigh range, is much longer than the width. The probe beam being collinear with the ODT beam images the trapped atoms along the beam direction at high optical density. The high-density atomic cloud induces a lensing effect in the absorption images when the probe beam detuning is $\approx \pm 50$ kHz from resonance. These images exhibit constructive interference of the imaging light in different regions of the image for detunings $+50$ and -50 kHz from resonance creating unsymmetric spectroscopy scans. This is solved by adding a linear model to the Voigt profile for the spectroscopy fits.

3. Fitting procedure

In Fig. 4, all of the black lines are related to the data collected. We fit a general quadratic model ($\alpha\lambda^2 + \beta\lambda + \gamma$) using a weighted least squares fitting procedure with the

weights given by $1/\text{DSSC}_{\text{err}}$ where DSSC_{err} is the error of each DSSC measurement. The 95% confidence interval is calculated using the error of the fit and a two-sided student- t value for 3° of freedom (≈ 3). The 95% prediction interval incorporates both the error of the fit and the error of the DSSC measurements using the same student- t value. We then use the 95% prediction interval to perform a Monte Carlo root finding method of the quadratic fit parameters with 10 000 iterations. The magic wavelength is given by the mean of all 10 000 iterations, and the error bar is given by the standard deviation. Thus, the 95% prediction interval will be ≈ 3 times greater than the magic wavelength error bar. The red theory curve is fit to the six data points leaving only the waist as a free parameter. The dashed-dot lines correspond to $\delta\alpha$ from the theoretical calculations plotted in Fig. 1.

4. Noise sources

The dominant noise source for the $m = 0$ measurements is the laser power variation of the ODT beam with power fluctuations below 2% over the time it takes to complete a single spectroscopy frequency scan. The $m = -1$ measurements are in addition affected by variations in intensity of the bias and background magnetic fields.

The electrical current generating the bias magnetic field is stabilized with a PID feedback controller and is stable for low-frequency noise up to 100 Hz. The entirety of the feedback system generates high-frequency peak-to-peak noise levels of 5 mV which, through the current transducer calibration and the magnetic coil setup, corresponds to a worst case fluctuation of ± 5 mG at frequencies greater than 100 Hz. Given the 2.1-kHz/mG Zeeman splitting under the magnetic-field bias, this generates a large noise source of ± 10.5 kHz which is evident in the noisier $m = -1$ DSSC data. The background field stability is below the measurable resolution of our external magnetometer of 10 mG, an AlphaLab VGM. Any long term drift of the magnetic field is accounted for by taking a second reference scan as mentioned in the text.

Our high-finesse WSU-2 wave meter is calibrated daily with our kHz-linewidth ≈ 689 -nm laser locked to the $^1S_0 - ^3P_1$ transition. At 473 nm, the ODT wavelength is beyond the calibration specification of the wave meter and, thus, induces a systematic offset in the wavelength reading. To measure this offset, we calibrate the wave meter to the $^1S_0 - ^1P_1$ transition at ≈ 461 nm and set our ODT wavelength to 473.000 000 nm. Then, we recalibrate it back to the 689-nm laser and note the ODT wavelength becomes 472.999 600 nm. Thus, we add an additional $+0.4$ -pm offset to our measured ODT wavelengths for both the $m = 0$ and the $m = -1$ data, which is an order of magnitude smaller than the smallest reported uncertainty of 4 pm.

5. θ_p Measurement

Any deviation of θ_p from 0° causes a systematic error as well as further uncertainty in the magic wavelength measurement. We measure the angle between the ODT polarization and the \vec{B}_{bias} field using an indirect measurement [28]. Since the probe beam and the ODT beam exist on the same plane, we ensure both beams are aligned to the same

axis, limited only by our measured extinction ratio of 18 dB. If the probe beam polarization is aligned to \vec{B}_{bias} ($\theta_p = 0^\circ$), there will only be excitation of the π transition. Alternatively, if the probe beam polarization is orthogonal to \vec{B}_{bias} ($\theta_p = 90^\circ$), there will only be excitation of the σ^- transition. Any deviation from $\theta_p = 0^\circ$ will cause a nonzero population in the

σ^- excitation. The excited-state populations are related to the Rabi frequency of each by $N_\pi = N_g \sin^2(\frac{t\Omega_\pi}{2})$ and similarly for σ^- . Expanding the $\sin(\cdot)$ terms yields a relationship between the population ratio and the ratio of Rabi frequencies. We deduce the angle offset by $\theta_p = \arctan(\frac{\Omega_{\sigma^-}}{\Omega_\pi})$

- [1] J. Ye, D. W. Vernooy, and H. J. Kimble, *Phys. Rev. Lett.* **83**, 4987 (1999).
- [2] B. J. Bloom, T. L. Nicholson, J. R. Williams, S. L. Campbell, M. Bishof, X. Zhang, W. Zhang, S. L. Bromley, and J. Ye, *Nature (London)* **506**, 71 (2014).
- [3] T. Ido and H. Katori, *Phys. Rev. Lett.* **91**, 053001 (2003).
- [4] M. Takamoto and H. Katori, *Phys. Rev. Lett.* **91**, 223001 (2003).
- [5] A. Cooper, J. P. Covey, I. S. Madjarov, S. G. Porsev, M. S. Safronova, and M. Endres, *Phys. Rev. X* **8**, 041055 (2018).
- [6] J. Ye, H. J. Kimble, and H. Katori, *Science* **320**, 1734 (2008).
- [7] S. Okaba, T. Takano, F. Benabid, T. Bradley, L. Vincetti, Z. Maizelis, V. Yampol'skii, F. Nori, and H. Katori, *Nat. Commun.* **5**, 4096 (2014).
- [8] A. D. Ludlow, M. M. Boyd, T. Zelevinsky, S. M. Foreman, S. Blatt, M. Notcutt, T. Ido, and J. Ye, *Phys. Rev. Lett.* **96**, 033003 (2006).
- [9] M. M. Boyd, A. D. Ludlow, S. Blatt, S. M. Foreman, T. Ido, T. Zelevinsky, and J. Ye, *Phys. Rev. Lett.* **98**, 083002 (2007).
- [10] M. S. Safronova, C. J. Williams, and C. W. Clark, *Phys. Rev. A* **67**, 040303(R) (2003).
- [11] M. Saffman and T. G. Walker, *Phys. Rev. A* **72**, 022347 (2005).
- [12] M. Saffman, *J. Phys. B: At., Mol. Opt. Phys.* **49**, 202001 (2016).
- [13] D. S. Weiss and M. Saffman, *Phys. Today* **70**(7), 44 (2017).
- [14] N. R. Hutzler, L. R. Liu, Y. Yu, and K.-K. Ni, *New J. Phys.* **19**, 023007 (2017).
- [15] J. P. Covey, I. S. Madjarov, A. Cooper, and M. Endres, *Phys. Rev. Lett.* **122**, 173201 (2019).
- [16] A. M. Kaufman, B. J. Lester, and C. A. Regal, *Phys. Rev. X* **2**, 041014 (2012).
- [17] M. Endres, H. Bernien, A. Keesling, H. Levine, E. R. Anschuetz, A. Krajenbrink, C. Senko, V. Vuletic, M. Greiner, and M. D. Lukin, *Science* **354**, 1024 (2016).
- [18] M. E. Kim, T.-H. Chang, B. M. Fields, C.-A. Chen, and C.-L. Hung, *Nat. Commun.* **10**, 1647 (2019).
- [19] T.-H. Chang, X. Zhou, M. Zhu, B. M. Fields, and C.-L. Hung, *Appl. Phys. Lett.* **117**, 174001 (2020).
- [20] J. S. Douglas, H. Habibian, C.-L. Hung, A. V. Gorshkov, H. J. Kimble, and D. E. Chang, *Nat. Photonics* **9**, 326 (2015).
- [21] C.-L. Hung, A. González-Tudela, J. I. Cirac, and H. J. Kimble, *Proc. Natl. Acad. Sci. USA* **113**, E4946 (2016).
- [22] A. Goban, K. S. Choi, D. J. Alton, D. Ding, C. Lacroute, M. Pototschnig, T. Thiele, N. P. Stern, and H. J. Kimble, *Phys. Rev. Lett.* **109**, 033603 (2012).
- [23] C. Lacroute, K. S. Choi, A. Goban, D. J. Alton, D. Ding, N. P. Stern, and H. J. Kimble, *New J. Phys.* **14**, 023056 (2012).
- [24] E. Vetsch, D. Reitz, G. Sagué, R. Schmidt, S. T. Dawkins, and A. Rauschenbeutel, *Phys. Rev. Lett.* **104**, 203603 (2010).
- [25] J. D. Thompson, T. G. Tiecke, N. P. de Leon, J. Feist, A. V. Akimov, M. Gullans, A. S. Zibrov, V. Vuletić, and M. D. Lukin, *Science* **340**, 1202 (2013).
- [26] T. G. Tiecke, J. D. Thompson, N. P. de Leon, L. R. Liu, V. Vuletić, and M. D. Lukin, *Nature (London)* **508**, 241 (2014).
- [27] M. Daly, V. G. Truong, C. F. Phelan, K. Deasy, and S. N. Chormaic, *New J. Phys.* **16**, 053052 (2014).
- [28] T. A. Zheng, Y. A. Yang, M. S. Safronova, U. I. Safronova, Z.-X. Xiong, T. Xia, and Z.-T. Lu, *Phys. Rev. A* **102**, 062805 (2020).
- [29] M. S. Safronova, S. G. Porsev, U. I. Safronova, M. G. Kozlov, and C. W. Clark, *Phys. Rev. A* **87**, 012509 (2013).
- [30] A. Kramida, Y. Ralchenko, J. Reader, and NIST ASD Team, NIST Atomic Spectra Database (ver. 5.9). Available: <https://physics.nist.gov/asd> Natl. Inst. Stand. Technol., Gaithersburg, MD. (2021).
- [31] M. Yasuda, T. Kishimoto, M. Takamoto, and H. Katori, *Phys. Rev. A* **73**, 011403(R) (2006).
- [32] A. Heinz, A. J. Park, N. Šantić, J. Trautmann, S. G. Porsev, M. S. Safronova, I. Bloch, and S. Blatt, *Phys. Rev. Lett.* **124**, 203201 (2020).
- [33] M. S. Safronova, M. G. Kozlov, W. R. Johnson, and D. Jiang, *Phys. Rev. A* **80**, 012516 (2009).
- [34] S. G. Porsev, Y. G. Rakhilina, and M. G. Kozlov, *Phys. Rev. A* **60**, 2781 (1999).
- [35] J. Mitroy, M. S. Safronova, and C. W. Clark, *J. Phys. B: At., Mol. Opt. Phys.* **43**, 202001 (2010).
- [36] S. G. Porsev, M. S. Safronova, and C. W. Clark, *Phys. Rev. A* **90**, 052715 (2014).
- [37] G. Kestler, Toward ultracold strontium on nanophotonics, Master's thesis, University of California, San Diego (2019).
- [38] S. Campbell, Ph.D. thesis, University of Colorado Boulder (2017).
- [39] T. L. Nicholson, S. L. Campbell, R. B. Hutson, G. E. Marti, B. J. Bloom, R. L. McNally, W. Zhang, M. D. Barrett, M. S. Safronova, G. F. Strouse, W. L. Tew, and J. Ye, *Nat. Commun.* **6**, 6896 (2015).
- [40] <https://udspace.udel.edu/handle/19716/29071>.
- [41] J. P. Bartolotta, M. A. Norcia, J. R. K. Cline, J. K. Thompson, and M. J. Holland, *Phys. Rev. A* **98**, 023404 (2018).
- [42] S. Snigirev, A. J. Park, A. Heinz, I. Bloch, and S. Blatt, *Phys. Rev. A* **99**, 063421 (2019).